Article:
Berry, AJ, Schofield, PF, Kravtsova, AN et al. (2017) The limitations of hibonite as a single-mineral oxybarometer for early solar system processes. Chemical Geology, 466. pp. 32-40. ISSN: 0009-2541

https://doi.org/10.1016/j.chemgeo.2017.03.031

The limitations of hibonite as a single-mineral oxybarometer for early solar system processes

Andrew J. Berry[1,2,3], Paul F. Schofield[3], Antonina N. Kravtsova[4], Laura A. Miller[2], Natasha R. Stephen[5], Andrew M. Walker[6], Alexander V. Soldatov[4], Trevor R. Ireland[1], K. Geraki[7], and J. Fred W. Mosselmans[7]

[1]Research School of Earth Sciences, Australian National University, Canberra, ACT, 2601, Australia

[2]Department of Earth Science and Engineering, Imperial College London, South Kensington, SW7 2AZ, UK

[3]Department of Earth Sciences, Natural History Museum, Cromwell Road, London, SW7 5BD, UK

[4]International Research Centre Smart Materials, Southern Federal University, Sorge 5, Rostov-on-Don, 344090, Russia

[5]Plymouth Electron Microscopy Centre, Plymouth University, Drake Circus, Plymouth, PL4 8AA, UK

[6]School of Earth and Environment, University of Leeds, Leeds, LS2 9JT, UK

[7]Diamond Light Source, Harwell Science and Innovation Campus, Didcot, OX11 0DE, UK

Abstract

The relationships between the composition of hibonite with the general formula $CaAl_{12-2x-y}Mg_xTi^{4+}_xTi^{3+}_yO_{19}$, the oxidation state of Ti ($Ti^{3+}/\Sigma Ti$, where $\Sigma Ti = Ti^{3+} + Ti^{4+}$), and oxygen fugacity ($fO_2$) were investigated experimentally. It was found that hibonite can be synthesised with a range of $Ti^{3+}/\Sigma Ti$ values at constant fO_2 and with a constant $Ti^{3+}/\Sigma Ti$ value for a range of fO_2s. It was also found that if hibonite with the formula $CaAl_{12-y}Ti^{3+}_yO_{19}$ ($Ti^{3+}/\Sigma Ti = 1$) is equilibrated with a melt of CAI composition at fO_2s below the iron-wüstite buffer then the resulting hibonite contained Mg, with Mg per formula unit (pfu) ~ 0.8 Ti pfu, and $Ti^{3+}/\Sigma Ti \sim 0.2$, irrespective of the fO_2. These results suggest that the availability of Mg, rather than fO_2, is the key factor that determines $Ti^{3+}/\Sigma Ti$ of hibonite. The structures of synthetic samples of hibonite with the general formula $CaAl_{12-2x}Mg_xTi^{4+}_xO_{19}$, where $0 \leq X < 1$, were determined by Rietveld refinement of X-ray powder diffraction data. The predominant site occupied by Ti^{4+} was found to change from M2 to M4 with increasing Ti

content. The range of Ti concentrations over which the site occupancy changed corresponds to that observed in meteoritic hibonite. This change in the Ti^{4+} site produces changes in the Ti K-edge XANES spectra, particularly in the intensity of the pre-edge feature, for constant $Ti^{3+}/\Sigma Ti$. The observed dependence of the pre-edge on the Ti^{4+} site was reproduced by *ab initio* simulations of the XANES spectra. The XANES spectra of natural hibonite with variable Ti content from the Murchison carbonaceous chondrite closely match the spectra of the synthetic samples with similar Ti contents. These differences in the spectra of meteoritic hibonite could be misinterpreted as being due to changes in $Ti^{3+}/\Sigma Ti$, but are instead due to differences in ΣTi, which relate to the petrogenetic history. Crystal chemistry exerts a first order control on the Ti site occupancy and $Ti^{3+}/\Sigma Ti$ value of hibonite. As a result, no simple relationship between $Ti^{3+}/\Sigma Ti$ and fO_2 should be expected. It is unlikely that hibonite will be useful as an oxybarometer for solar processes without $Ti^{3+}/\Sigma Ti$ standards that are compositionally matched to the unknown.

Key Words

hibonite, calcium hexaluminate, CA6, CAI, oxybarometry, solar nebula, crystal chemistry, oxygen fugacity, XANES, FDMNES

Introduction

Hibonite ($CaAl_{12}O_{19}$) is the second mineral, after corundum, to condense from a gas of solar composition (Kornacki and Fegley 1986; Yoneda and Grossman 1995; Lodders 2003). It incorporates varying amounts of Ti as both Ti^{3+} and Ti^{4+}. Ti^{3+} substitutes directly for Al^{3+} whereas Ti^{4+} undergoes a charge coupled substitution with Mg^{2+} ($Ti^{4+} + Mg^{2+} = 2Al^{3+}$). A general formula for Ti-bearing hibonite is $CaAl_{12-2x-y}Mg_xTi^{4+}{}_xTi^{3+}{}_yO_{19}$. There are five Al sites in hibonite (M1-M5) and their multiplicity and coordination numbers are given by $^{[12]}Ca^{[6]}M1^{[5]}M2^{[4]}M3_2{}^{[6]}M4_2{}^{[6]}M5_6O_{19}$ (where coordination numbers are superscripted in square brackets and the multiplicity of the site is subscripted). It has been shown recently by neutron powder diffraction (NPD) of synthetic hibonite, and density functional theory (DFT), that Ti^{3+} occupies adjacent face-sharing octahedral M4 sites due to a stabilising Ti-Ti interaction, Ti^{4+} occupies both the M2 and M4 sites (~ 1:5 at 1400 ˚C) with the occupancy of M4 again stabilised by a Ti-Ti interaction, and Mg occupies the tetrahedral M3 site and Mg-Ti interactions are not important (Doyle et al. 2014). These site occupancies are broadly consistent with results obtained by single-crystal X-ray diffraction (Giannini et al. 2014). In dilute systems, where Ti is present as isolated cations, Ti^{3+} is predicted to occupy M2, Ti^{4+} the M2 site, and Mg^{2+} the M3 site (Doyle et al. 2014).

It has been proposed that the ratio of Ti^{3+} to Ti^{4+} in hibonite, given as $Ti^{3+}/\Sigma Ti$ where $\Sigma Ti = Ti^{3+} + Ti^{4+}$, may record the oxygen fugacity (fO_2) at the time of crystallisation/condensation from the solar nebula or of a later reprocessing event (Ihinger and Stolper 1986; Beckett et al. 1988). The presence of Ti^{3+} results in a blue colour that is often considered to be diagnostic of meteoritic hibonite and the intensity of the absorption band that gives rise to this colour has been used to provide constraints on the fO_2 at which crystals equilibrated (Ihinger and Stolper 1986). $Ti^{3+}/\Sigma Ti$ in hibonite has been quantified from the intensity of the electron spin resonance (ESR) signal arising from the unpaired electron in Ti^{3+}, and values of ~ 0.2 were obtained for samples from the Murchison carbonaceous chondrite (Beckett et al. 1988), however, relating $Ti^{3+}/\Sigma Ti$ to fO_2 was compromised by the uncertain Ti site occupancies. These attempts to determine fO_2 using hibonite gave values that were either poorly constrained or significantly more oxidised than expected.

X-ray absorption near edge structure (XANES) spectroscopy is a technique that allows oxidation state ratios to be determined with micron spatial resolution and a precision of ± 1% (absolute) (e.g. Berry et al. 2008, 2010). It has been used to determine the Ti site and oxidation state in minerals (e.g. Berry et al. 2007; Simon et al. 2007; Tailby et al. 2011).

Spatially-resolved soft X-ray spectroscopies such as X-ray photo-emission electron microscopy (XPEEM) and scanning transmission X-ray microscopy (STXM) also have the potential to accurately quantify oxidation states and image their distribution (Schofield et al. 2014). Integral to correctly interpreting the results of any spectroscopic technique in terms of $Ti^{3+}/\Sigma Ti$ is an understanding of the crystal chemistry, since cations with the same oxidation state at different crystallographic sites can give different spectra.

Here we present the results of three sets of experiments on the roles of crystal chemistry and fO_2 on the $Ti^{3+}/\Sigma Ti$ value of hibonite and hence the suitability of hibonite as a single mineral oxybarometer. Firstly, the site occupied by Ti^{4+} in hibonite with the general formula $CaAl_{12-2x}Mg_xTi^{4+}_xO_{19}$ (i.e. $Ti^{3+}/\Sigma Ti = 0$) was determined for variable ΣTi by Rietveld refinement of X-ray diffraction (XRD) data. XANES spectra of these samples were compared to those predicted for Ti^{4+} at different defect sites and those of meteoritic hibonite. Secondly, hibonite with the general formula $CaAl_{12-y}Ti^{3+}_yO_{19}$ (i.e. $Ti^{3+}/\Sigma Ti = 1$) was equilibrated with a melt of calcium-aluminium inclusion (CAI) composition, at different fO_2s. These experiments were designed to simulate possible reactions between early-formed hibonite and further condensate or melt in the solar nebula. Thirdly, oxides corresponding to hibonite with the general formula $CaAl_{12-2x-y}Mg_xTi^{4+}_xTi^{3+}_yO_{19}$ were equilibrated at 1400 ˚C to determine the fO_2 range over which hibonite with a particular $Ti^{3+}/\Sigma Ti$ value can be synthesised.

Experimental

Samples are identified by reference to their Ti per formula unit (pfu) and $Ti^{3+}/\Sigma Ti$ ratios using the notation (Ti pfu, $Ti^{3+}/\Sigma Ti$). For example, the sample (1.0, 1.0) will have 1.0 Ti pfu and all the Ti will be Ti^{3+} giving a chemical formula of $CaAl_{11.0}Ti_{1.0}O_{19}$. The sample (1.0, 0.0) will have 1.0 Ti^{4+} pfu (and 1.0 Mg^{2+} pfu) giving a chemical formula of $CaAl_{10.0}Ti_{1.0}Mg_{1.0}O_{19}$.

To investigate the effect of different amounts of Ti^{4+} on the structure of hibonite, samples with the compositions (0.0, 0.0), (0.1, 0.0), (0.2, 0.0), (0.3, 0.0) and (0.4, 0.0) (i.e. the general formula $CaAl_{12-2x}Mg_xTi^{4+}_xO_{19}$) were prepared from stoichiometric mixtures of $CaCO_3$, Al_2O_3, $(NH_4)_2TiO(C_2O_4)_2.nH_2O$ ($n \sim 1$; ammonium titanium oxalate or ammonium bis(oxalato)oxotitanate(IV) hydrate, CAS 10580-03-7) and $Mg(NO_3)_2.nH_2O$ ($n \sim 6$). $(NH_4)_2TiO(C_2O_4)_2.nH_2O$ and $Mg(NO_3)_2.nH_2O$ were standardised by firing at 1000 ˚C to determine the yields of TiO_2 and MgO, respectively. $(NH_4)_2TiO(C_2O_4)_2.nH_2O$ is soluble in

126 water, and $Mg(NO_3)_2.nH_2O$ is soluble in both water and acetone, and solutions of each were
127 added separately to a mixture of $CaCO_3$ and Al_2O_3 and stirred until the solvent evaporated.
128 The addition of Ti and Mg in solution ensures that these elements, which are present at low
129 concentrations, are homogeneously distributed in the resulting mix. The mix was pressed into
130 a pellet and heated at 1400 ˚C (the incongruent melting point of $CaAl_{12}O_{19}$ is 1852 ˚C;
131 Jerebtsov and Mikhailov 2001) in an atmosphere of CO_2 (corresponding to an fO_2 of +6.7 log
132 units relative to the iron-wüstite, IW, buffer) for 24 h, cooled to 600 ˚C, reground, and re-
133 heated at 1400 ˚C for a further 24 h. Samples of (0.44, 0.0), (0.98, 0.0), and (0.20, 1.0) were
134 prepared previously from mixtures of $CaCO_3$, Al_2O_3, TiO_2, and MgO (Doyle et al. 2014).
135
136 To investigate changes in hibonite composition due to equilibration with a melt, samples of
137 Ti^{3+} hibonite were prepared from mixtures of $CaCO_3$, Al_2O_3, and $(NH_4)_2TiO(C_2O_4)_2.nH_2O$
138 ((0.15, 1.0) and (0.25, 1.0)), or $CaCO_3$, Al_2O_3, and TiO_2 ((0.30, 1.0)), in equilibrium with
139 graphite and CO at 1400 ˚C, powdered, and mixed with either composition Hib2Ti5 of
140 Beckett and Stolper (1994) (SiO_2 21.18, TiO_2 4.85, MgO 3.35, Al_2O_3 44.53, CaO 26.55, all as
141 wt%, called A, prepared from oxides and $CaCO_3$) or a modified version of this composition
142 without TiO_2 (called B), in the proportions 40% hibonite, 60% Hib2Ti5 (by wt). The
143 composition Hib2Ti5 was chosen because it gives melt and hibonite at ~ 1450 ˚C over an fO_2
144 range from at least IW-3.3 to IW+6.6. The resulting powders were mixed with polyethylene
145 oxide and water to form a paste, which was mounted on wire loops, and equilibrated at 1450
146 ˚C and values of $\log fO_2$ corresponding to IW-0.3, -1.3, -2.3, -3.3, and -4.3. The loops were
147 made of Pt for IW-0.3, -1.3, and -2.3, and Re for IW-3.3 and -4.3. The fO_2 was controlled
148 using mixtures of CO and CO_2. Powders were also pressed into a pellet and equilibrated with
149 graphite and CO (IW-6.3). After at least 24 h the samples were quenched in water (see
150 Burnham et al. 2015 for further experimental details).
151
152 To investigate the fO_2 stability range of hibonite, mixtures of oxides corresponding to the
153 hibonite compositions (0.98, 0.0), (0.62, 0.6), and (0.33, 1.0) were pressed into pellets and
154 heated at 1400 ˚C and values of $\log fO_2$ equal to IW-6.3, -2.3, -0.3, +2.3, +4.3, +7.3, as
155 described above, for ~ 24 h. All samples were held in Pt wire baskets except for those at IW-
156 6.3, which were in graphite.
157
158 Portions of all samples were mounted in epoxy resin and polished for imaging and XANES
159 spectroscopy. Portions were also powdered for quantitative phase analysis and structural
160 characterisation using XRD. Samples of hibonite from the Murchison carbonaceous
161 chondrite (Ireland 1988, 1990) were presented as crystal fragments pressed into gold (Ireland

et al. 1992).

High-spatial-resolution back-scattered electron (BSE) images and elemental maps were acquired using a JEOL 7001 FE-SEM, operating at 15 kV and a working distance of 10 mm, with AZtec software (Oxford Instruments). Compositions were determined using a Cameca SX-100 electron probe (EPMA), operating at 15 kV and 20 nA, with LTAP (for Si, Mg and Al) and PET (for Ca and Ti) crystals. Wollastonite (for Si and Ca), forsterite (Mg), corundum (Al) and synthetic $MnTiO_3$ (Ti) were used as standards and the detection limits (wt%) were 0.02 for Si, Mg and Al, 0.05 for Ca, and 0.04 for Ti.

XRD patterns were collected using a θ/2θ PANalytical X'Pert Pro α1 X-ray diffractometer with an X'celerator real-time strip-detector that has an active detector length of 2.122 °. Data for quantitative phase analysis (QPA) and structural characterisation were collected using Cu Kα and Cu $K\alpha_1$ radiation, respectively. For QPA, data were collected from powdered samples on kapton film, in transmission geometry, between 5 and 97 º2θ using a step size of 0.017 º and a scan rate of 0.001 $^{\circ}s^{-1}$, resulting in total scan times of ~ 23 h. For structural characterisation, data were collected from powdered samples packed into a top-loaded deep-well sample holder, in reflection geometry, between 5 and 125 º2θ using a step size of 0.017 º and a scan rate of 0.0056 $^{\circ}s^{-1}$, resulting in total scan times of ~ 6 h. The samples were spun in the plane of the sample surface during data collection in both geometries. The resulting patterns were analysed by Rietveld refinement within the GSAS (General Structure Analysis System) code of Larson and Von Dreele (1994) interfaced with EXPGUI (Toby 2001). For both the QPA and crystal structure refinements the starting models used data for Ti-bearing hibonite from Doyle et al. (2014). For the QPA, peak profiles (type 2) were modelled using the model-dependent Le Bail method and the backgrounds using a six-term power series function. Phases were identified by pattern matching using the JCPDS database of the International Centre for Diffraction Data. Phase proportions were quantified using the Rietveld method in which the scale factor, phase fractions and cell parameters were refined simultaneously. The unit cell parameters were allowed to vary but no attempt was made to iterate the site occupancies. The refinements were constrained to maintain chemical mass balance such that the final chemistry closely matched the composition of the original oxide mix. The final refinement sequences included a six-term, spherical-harmonic preferred orientation parameter for hibonite. For the crystal structure refinements, peak profiles (type 2) were also modelled using the Le Bail method but the backgrounds used a four-term power series function. The structural parameters of additional phases (if any) were added, the diffraction patterns were scaled, and then all phases were refined simultaneously. For

198 hibonite, the unit-cell parameters were refined first, followed by the atomic coordinates and
199 atomic displacement parameters (ADP). The Ti (and Mg by stoichiometry) site occupancies
200 were fixed during the least squares refinements and manually iterated between refinement
201 cycles.
202
203 Titanium K-edge XANES spectra were recorded at I18 of Diamond Light Source
204 (Mosselmans et al. 2009). The excitation energy was selected using a Si(111)
205 monochromator and calibrated by defining the first derivative peak of a Ti foil spectrum to be
206 at 4966.4 eV. The energy resolution at the Ti K-edge was 0.70 eV, which when coupled with
207 the Ti Kα core-hole width of 0.94 eV resulted in a spectral resolution of 1.2 eV. High-energy
208 harmonics were removed by Rh coated KB mirrors that were used to focus the beam to ~ 3 x
209 3 μm. The penetration depth of Ti K-edge X-rays (absorption length) in $CaAl_{12}O_{19}$ is ~ 17
210 μm. Fluorescence was detected using either a nine-element Ge or a four-element Si drift
211 (Vortex) detector and the distance between the detector and sample was adjusted to ensure
212 that the total incoming count rate was within the linear range of the signal processing
213 electronics. Samples were mounted at 45˚ to both the incident beam and the detector. Spectra
214 were recorded from 4950-5200 eV with a step size of 0.5 eV for the baseline (4950-4960 eV),
215 0.1 eV for the pre-edge (4960-4975), 0.2 eV for the edge (4975-5015) and 2.5 eV above the
216 edge. The total spectral acquisition time was ~ 20 min. The Ti Kα fluorescence intensity was
217 dead-time corrected, normalised to the intensity of the incident beam, and the resulting
218 spectra compared after subtraction of a constant baseline and normalisation to the average
219 intensity above 5145 eV. For the synthetic samples spectra were recorded from a number of
220 points. Spectra of meteoritic crystals were recorded for random orientations.
221
222 The Ti K-edge XANES spectra of Ti^{3+} and Ti^{4+} occupying various sites in hibonite were
223 simulated using the full-potential finite difference method to solve the Schrödinger equation
224 in real space while accounting for the core hole created by the electronic transition. The
225 simulations made use of the FDMNES program (Joly 2001, Bunau and Joly 2009) and the
226 Hedin-Lundquist exchange-correlation potential. Atomic geometries corresponding to the
227 different defects used in the simulations were taken from the DFT calculations described in
228 Doyle et al. (2014). Specifically, spectra were calculated for isolated Ti^{3+} on M2, isolated
229 Ti^{4+} on either M2 or M4, and clusters of either two Ti^{3+} or two Ti^{4+} on adjacent face-sharing
230 M4 sites. Ti^{4+} was charge balanced by Mg^{2+} on M3. These geometries correspond to models
231 $Ti_{Al(2)}^{\times}$, $\{Ti_{Al(2)}^{\bullet}Mg_{Al(3)}^{\prime}\}_b$, $\{Ti_{Al(4)}^{\bullet}Mg_{Al(3)}^{\prime}\}$, $\{Ti_{Al(4)}^{\times}Ti_{Al(4)}^{\times}\}$ and
232 $\{Ti_{Al(4)}^{\bullet}Ti_{Al(4)}^{\bullet}Mg_{Al(3)}^{\prime}Mg_{Al(3)}^{\prime}\}$, respectively, in Tables 5 and 6 of Doyle et al. (2014). For
233 each model a spherical atomic cluster of radius 5.6 Å around the central Ti cation was

extracted from the periodic model (previously subjected to geometry optimisation using DFT) and this finite cluster was used for the simulation of the XANES spectra. The calculated spectra were arbitrarily shifted in energy in order to align them with the experimental spectra.

Results

The $CaAl_{12-2x}Mg_xTi^{4+}_xO_{19}$ samples (i.e. those prepared at 1400 ˚C and IW+6.7) were white, polycrystalline aggregates (crystals ~ 5 μm), and were either phase pure within the detection limits of XRD or contained traces (< 2 wt%) of Al_2O_3. The lattice parameters and site occupancies determined by Rietveld refinement of the XRD data are given in Table 1. This includes new data for samples (0.44, 0.0) and (0.98, 0.0) for which the structures have been determined previously using NPD data (Doyle et al. 2014). The dependencies of the *c* lattice parameter and unit cell volume on Ti content for these samples, and determined by NPD (Doyle et al. 2014) and X-ray single-crystal diffraction (Giannini et al. 2014) for samples with a range of $Ti^{3+}/\Sigma Ti$ values, are shown in Figure 1. The *a* lattice parameter (not plotted) exhibits a similarly good correlation with Ti pfu. Ti was found to only occupy the M2 and M4 sites in agreement with previous studies (Doyle et al. 2014, Giannini et al. 2014). There is one M2 site, which is split into two symmetrically equivalent half-occupied sites by the static displacement of the M2 cation from the site-centre, and two M4 sites pfu. Therefore, Ti pfu due to M2 and M4 is equal to twice the occupancy (as presented in Table 1) and M2/M4 in terms of occupancy is equivalent to M2/M4 in pfu. The Ti^{4+} M4 site occupancy was either determined directly (for samples in which all Ti is assumed to be Ti^{4+}) or calculated by assuming that the total Ti^{4+} pfu is equal to Mg^{2+} pfu and all Ti on M2 is Ti^{4+} (Doyle et al. 2014). Ti^{4+} on the M4 site pfu and the Ti^{4+} M2/M4 site occupancy ratio, as a function of Ti^{4+} pfu, are shown in Figure 2.

All the hibonite-melt samples were blue. BSE images and elemental maps for representative samples are shown in Figure 3. The BSE images of all samples show two types of euhedral crystals: blocky crystals (5-15 μm), which often exhibit hexagonal symmetry and are clearly zoned (rims ~ 1 μm), and elongate or lathe-like crystals (3-5 μm). The lathes and the rims of the zoned crystals are similar in the BSE images and are enriched in Ti and Mg relative to the cores (Fig. 3b). The correlation between the BSE images and the elemental maps suggests that the zoning is real and not an edge effect. The elemental maps also show that hibonite crystals that were originally Mg-free ($CaAl_{12-y}Ti^{3+}_yO_{19}$) contain significant Mg after

equilibration with the melt; the distribution of Al distinguishes hibonite from melt (Fig. 3d), Ti is enriched in the crystals relative to what was initially a Ti-free melt (Fig. 3e), and Mg is almost uniformly distributed between hibonite and melt (Fig. 3f). The compositions of the crystals determined by EPMA are given in Table 2. The size of the crystals makes it difficult to obtain analyses that do not contain a contribution from the surrounding quenched melt. In many cases analyses were obtained for a series of points traversing a crystal in the hope of identifying a point for which the melt contribution was minimal. The Si content was used as an indicator of melt since hibonite contains a small or negligible amount (Beckett and Stolper 1994) whereas the melt contains over 20 wt% SiO_2. An example traverse is shown in Figure 4 where the Si content reaches a minimum value in the centre of a crystal. For many samples it was not possible to obtain analyses of hibonite that were not contaminated by the melt and only the analysis with the lowest SiO_2 value, if also less than 1.0 wt% (average ~ 0.4 wt%), is reported in Table 2. Thus, these results are for the subset of samples for which the analyses are considered reliable. For some samples two different hibonite compositions were obtained and both are given in Table 2. The SiO_2 contents are consistent with values reported previously for hibonite (Beckett and Stolper 1994; Simon et al. 1997), but if they were to arise from the surrounding melt the associated contribution to the Mg and Ti contents of the hibonite would be less than 0.1 wt%. The independence of the Si and Mg concentrations shown in Figure 4 indicates that the Mg in the crystal is not an artefact attributable to the melt.

The oxide compositions corresponding to (0.98, 0.0), (0.62, 0.6), and (0.33, 1.0) produced polycrystalline hibonite at 1400 ˚C and all values of fO_2 (IW-6.3 to IW+7.3), plus varying amounts of $CaTiO_3$, $MgAl_2O_4$, Al_2O_3, Al_2TiO_5, and Ti-oxides. The hibonite lattice parameters and the phase proportions of each sample are given in Table 3, and the variations of the *c* lattice parameter and wt% of hibonite as a function of fO_2 are shown in Figure 5. It is not possible to distinguish Mg from Al using XRD data and hence site occupancies and $Ti^{3+}/\Sigma Ti$ could not be determined for these samples. The powdered products were a shade of blue for all three compositions at fO_2s equal to and below IW+4.3, while the product of composition (0.62, 0.6) was also blue at IW+7.3.

Ti K-edge XANES spectra recorded from different points on each $CaAl_{12-2x}Mg_xTi^{4+}{}_xO_{19}$ sample were essentially identical. Spectra recorded from a randomly oriented single crystal as a function of orientation to the X-ray beam were also essentially identical (Doyle et al. 2016). Spectra for samples (0.1, 0.0) and (0.44, 0.0) are shown in Figure 6(b, d). Also shown are spectra for two hibonite crystals from the Murchison carbonaceous chondrite (10-43 and

7-981), which are typical of two spectral types that were observed for a number of crystal fragments. Sample 10-43 (Blue AGregate or BAG) contains 6.44 wt% TiO_2 (0.55 Ti pfu) and has the formula $Ca_{1.03}Al_{10.93}Mg_{0.48}Ti_{0.55}O_{19}$, while 7-981 (PLAty Crystal or PLAC) contains 1.19 wt% TiO_2 (0.1 Ti pfu) and corresponds to $Ca_{1.01}Al_{11.78}Mg_{0.12}Ti_{0.10}O_{19}$ (Ireland 1988). The pre-edge region for these two samples, for synthetic samples with $Ti^{3+}/\Sigma Ti = 0$ but varying Ti pfu, and a synthetic sample with $Ti^{3+}/\Sigma Ti = 1$ (Doyle et al. 2016) are shown in Figure 7. Spectra of other Murchison crystals, and hibonite in CAIs from various R3, CR2, and unique meteorites will be presented elsewhere.

Ti K-edge XANES spectra for hibonite with Ti^{3+} and Ti^{4+} at various substitutional sites, modelled using FDMNES, are shown in Figure 8. The pre-edge regions of the Ti^{4+} models are shown in Figure 9 along with the spectrum of sample 10-43. In both figures the spectrum resulting from a linear combination of the spectra for Ti^{4+} on M2 and Ti^{4+} clustered on M4, in a proportion similar to that predicted by XRD and NPD for hibonite with a Ti pfu comparable to that of 10-43, is also shown.

Discussion

Hibonite containing only Ti^{4+} is colourless (appears white), that containing only Ti^{3+} is grey or blue, while mixed valent samples containing both Ti^{3+} and Ti^{4+} are deep blue. The blue colour arises from the d^1 electronic configuration of Ti^{3+} and may correspond to either a *d-d* transition or charge transfer between Ti^{3+} and Ti^{4+}, noting that such an interaction has been reported for Ti in Al_2O_3 (Yamaga et al. 1994) and that Ti^{3+} and Ti^{4+} may occupy neighbouring, face-sharing M4 octahedra in hibonite. The colour blue is considered to be diagnostic of hibonite in CAIs (Ireland 1988) and the presence of Ti^{3+} is generally taken to imply that crystals formed or equilibrated under reduced conditions.

$Ti^{3+}/\Sigma Ti$ in a melt will have a sigmoidal dependence on fO_2 (see Berry and O'Neill 2004). If hibonite crystallises from a condensate (a low density melt) then $Ti^{3+}/\Sigma Ti$ in hibonite should be related to $Ti^{3+}/\Sigma Ti$ in the condensate. However, the partition coefficients of Ti^{3+} and Ti^{4+} will be different and the uptake of Ti^{4+} will depend on the availability of Mg (for charge balance). In the absence of Mg all Ti in hibonite must be Ti^{3+} (i.e. $Ti^{3+}/\Sigma Ti = 1$), irrespective of the fO_2, and the amount of Ti will depend on the activity of Ti^{3+} in the condensate or melt. In the synthesis of mixed-valent samples from oxides a range of $Ti^{3+}/\Sigma Ti$ values (= 0.27, 0.33,

0.39. 0.60, and 1.0) were all prepared at constant fO_2 (IW-6.3) by varying the amount of Mg (Doyle et al. 2014). The Mg pfu required a stoichiometric amount of Ti to be Ti^{4+} with any Ti pfu > Mg pfu attributed to Ti^{3+}. Determining $Ti^{3+}/\Sigma Ti$ in these samples would thus provide no insight into the fO_2 of formation.

The role of crystal chemistry was investigated further in this study by the experiments in which oxide compositions corresponding to hibonites containing only Ti^{3+}, only Ti^{4+}, and both Ti^{3+} and Ti^{4+} were heated at 1400 ˚C and values of fO_2 corresponding to IW-6.3 to +7.3. For each composition the lattice parameters of the hibonite were similar at all fO_2s (Fig. 5a), despite the sensitivity of the parameters to ΣTi (Fig. 1) and Ti^{4+} pfu (Doyle et al. 2014). Although the Ti^{3+} composition yielded a large proportion of impurity phases at all fO_2s other than the most reduced, hibonite was always the dominant phase for the other two compositions (Fig. 5b; Table 3). Indeed, the mixed valent composition produced almost phase pure hibonite over the entire fO_2 range with very little change in the lattice parameter i.e. hibonite with $Ti^{3+}/\Sigma Ti = 0.6$ was prepared over 13 log units in fO_2. This suggests that crystal chemistry stabilises Ti^{3+} and Ti^{4+} to significantly more oxidised and reduced conditions, respectively, than might be expected. Thus, a range of $Ti^{3+}/\Sigma Ti$ values can be produced at a single fO_2 and a constant $Ti^{3+}/\Sigma Ti$ value can be produced for a range of fO_2s.

Melt composition A at 1450 ˚C should produce hibonite and melt (Beckett and Stolper 1994). Therefore, the equilibration experiments between hibonite and melt A might be expected to yield two generations of hibonite: the pre-synthesised starting material after equilibration with the melt and liquidus crystals. Melt composition B (Ti-free) was chosen to suppress the formation of liquidus hibonite. The large blocky crystals are attributed to the pre-synthesised hibonite and the small lathe-like crystals and rims on the blocky crystals to hibonite that crystallised from the melt, either at the experimental conditions or on quenching. All experiments produced both generations of hibonite, including those with melt B, indicating that the pre-synthesised hibonite partially dissolved in melt B to produce a modified melt that crystallised new hibonite. This is consistent with the presence of Ti in the quenched melts. The composition of the pre-synthesised hibonite was of the form $CaAl_{12-y}Ti^{3+}_yO_{19}$ yet all the hibonite analyses in Table 2 contain Mg in an amount approximately equal to that of Ti, in pfu. The Mg, as illustrated in Figure 4, is unambiguously present in the hibonite and can not be attributed to fluorescence derived from the surrounding melt. The presence of Mg, seemingly homogeneously distributed in the crystals, is shown in Figure 3f. For some samples different hibonite compositions are reported in Table 2 and these are attributed to the

re-equilibrated and liquidus crystals, however, all have Ti pfu ~ Mg pfu. The Ti pfu in some cases corresponds closely to that of the pre-synthesised hibonite. In other cases the crystal analysed could have grown from the melt or represent a composition closer to crystal-melt equilibrium. The key point is hibonite crystals that contained Ti only as Ti^{3+} have incorporated Mg during equilibration with a melt and as a result now contain Ti as predominantly Ti^{4+}, at all fO_2s. The average value of $Ti^{3+}/\Sigma Ti$ calculated from stoichiometry is 0.09(8), assuming Ti^{4+} pfu = Mg pfu, or 0.30(11) if Ti^{4+} + Si pfu = Mg pfu (Mg^{2+} may be charge balanced by both Ti^{4+} and Si^{4+}; Simon et al. 1997). The correlation between Mg and Ti + Si pfu is shown in Figure 10 and has a slope of ~ 0.8. If Ti pfu is converted to Ti^{4+} pfu using the average value of $Ti^{3+}/\Sigma Ti$ then the slope of the correlation is ~ 1. The ratio of Mg to Ti + Si is constant and independent of fO_2. The correlation between Mg and Ti also has a slope of ~ 0.8 but does not pass through 0 (intercept 0.02). Equilibration of hibonite with a melt of CAI composition results in the uptake of Mg and, for charge balance, a stoichiometric amount of Ti^{3+}must be oxidised to Ti^{4+}, even at IW-6.3. This suggests that the Mg activity of the melt, and hence crystal chemistry, is more important for determining the $Ti^{3+}/\Sigma Ti$ value of hibonite than fO_2. These experiments were designed to simulate the equilibration of crystallised/condensed hibonite with further condensate or melt and it is noted that the $Ti^{3+}/\Sigma Ti$ values obtained are similar to those estimated for hibonite from the Murchison carbonaceous chondrite (0.15-0.28; Beckett et al. 1988).

The condensation temperatures of the major elements, for a gas of solar composition at a pressure of less than 0.01 atm, decrease in the order Al, Ca, Ti, Si, Mg, Fe (Lodders 2003). Corundum is the first phase to condense (Yoneda and Grossman 1995) and may contain up to 0.25 wt% Ti (Simon et al. 2002), most likely as Ti^{3+}. With continued cooling and condensation corundum is believed to react with Ca to form hibonite. Accordingly, corundum-bearing CAIs are rare and corundum has been found enclosed by hibonite (Simon et al. 2002; Nakamura et al. 2007). The first meteoritic hibonite to condense might be expected to have the composition $CaAl_{12-y}Ti_yO_{19}$. Further condensation would make Mg available to the system. If Mg was to equilibrate with hibonite, which at that point would contain Ti as only Ti^{3+}, then Ti^{3+} must oxidise to Ti^{4+} in order for the Mg to be accommodated. If new hibonite that contains Mg was to crystallise then it must also contain Ti^{4+}. The addition of Mg and Ti from a melt to early-formed meteoritic hibonite has been proposed as a mechanism for producing rims of secondary hibonite with different Mg:Ti ratios and colours (Simon et al. 1997). Meteoritic hibonite with small blue cores surrounded by thick colourless rims have been observed (Rout and Bischoff 2008). The difference in

colour was attributed to differences in the Ti content but could also be due to differences in Mg content and hence Ti oxidation state, noting a strong 1:1 correlation between Mg pfu and Ti pfu overall but Ti > Mg for the blue components. This 1:1 correlation, which is a general characteristic of meteoritic hibonite (see Doyle et al. 2014), the ability to synthesise hibonite under reduced conditions with almost any $Ti^{3+}/\Sigma Ti$ depending on the available Mg, and the fact that hibonite with $Ti^{3+}/\Sigma Ti = 1$ will gain Mg during equilibration with a CAI melt composition resulting in $Ti^{3+}/\Sigma Ti \sim 0.2$, independently of fO_2 (at least below IW), indicate that stoichiometry, or the activity of Mg, is more important for controlling $Ti^{3+}/\Sigma Ti$ than fO_2.

The lattice parameters and unit cell volumes determined by X-ray powder diffraction (Table 1) are consistent with those of other studies (Fig. 1). The increase with Ti pfu is mainly due to the corresponding increase in Mg pfu and the larger size of Mg^{2+} relative to Al^{3+} (Doyle et al. 2014). XRD provides excellent contrast between Al and Ti and the occupancies of Ti^{4+} on M4 (Fig. 2a) as a function of Ti^{4+} pfu are similar to those determined by NPD and single-crystal XRD (Doyle et al. 2014; Giannini et al. 2014). The slope of the correlation is less than 1 (~ 0.8) because Ti^{4+} also occupies the M2 site. The ratio of the Ti^{4+} occupancy of M2 and M4 (Fig. 2b) determined in this study varies systematically with Ti^{4+} pfu. At low concentrations Ti^{4+} predominantly occupies the M2 site, as predicted by DFT for isolated cations, while at higher concentrations Ti^{4+} prefers the M4 site due to the stabilising Ti-Ti interaction that occurs if adjacent M4 sites are occupied (Doyle et al. 2014). All the data are in general agreement with the trend, although the mixed-valent sample with the highest value of $Ti^{3+}/\Sigma Ti$ (0.62, 0.60) has an unexpectedly low Ti^{4+} M2/M4 value, which may indicate a stabilising Ti^{3+}(M4)-Ti^{4+}(M4) interaction that results in Ti^{4+} occupying M4 even at low Ti^{4+} pfu.

The Ti K-edge XANES spectra of the (0.1, 0.0) and (0.44, 0.0) synthetic samples are very similar (pre-edge, edge, and post-edge) to those of natural samples 7-981 (0.1 Ti pfu) and 10-43 (0.55 Ti pfu), respectively (Fig. 6). This is shown in more detail for the pre-edge in Figure 7. For the samples with $Ti^{3+}/\Sigma Ti = 0$ the pre-edge systematically decreases in maximum intensity and broadens (develops shoulders at lower and higher energies) with increasing Ti^{4+} pfu (from ~ 0.1 to 1.0). Over this range Ti^{4+} changes site from M2 to predominantly M4. The pre-edge feature corresponds to the 1s→3d transition, which is forbidden in octahedral coordination, but may gain intensity by orbital mixing in lower symmetry environments. Accordingly, for Ti^{4+}, the pre-edge intensity has been shown to increase from $^{[6]}$Ti to $^{[5]}$Ti to $^{[4]}$Ti coordination (Farges et al. 1996). In hibonite a change in site symmetry from trigonal

445 bipyramidal ($^{[5]}$M2) to octahedral ($^{[6]}$M4) should therefore be associated with a decrease in
446 pre-edge intensity, as observed. The pre-edge region of 7-981 is consistent with most of the
447 Ti^{4+} occupying the M2 site (compare b and c in Fig. 7) and that of 10-43 with Ti^{4+} occupying
448 both M2 and M4 (compare a and f in Fig. 7). The effect of what would be a small (from
449 stoichiometry) amount of Ti^{3+} in 10-43 on the pre-edge is insignificant given the shape of the
450 pre-edge for (0.2, 1.0) shown in Figure 7h. Changes in Ti^{4+} site occupancy with changes in
451 concentration, at constant fO_2, produce changes in the XANES spectra that could easily be
452 misinterpreted as being due to changes in $Ti^{3+}/\Sigma Ti$. The XANES spectra of meteoritic
453 hibonite differ with ΣTi, which relates to the petrogenetic history, and the effect of differences
454 in Ti site occupancy will be convolved with any differences in $Ti^{3+}/\Sigma Ti$.
455
456 The large effect of the Ti^{4+} site occupancy on the pre-edge is confirmed by the XANES
457 models shown in Figure 9. The pre-edge for Ti^{4+} on M2 is significantly more intense, and
458 less structured than that for Ti^{4+} on M4, either as an isolated cation or as a cluster. The Ti^{4+}
459 site occupancy of sample 10-43 is expected to be around 20% M2 and 80% M4 and the
460 simulated spectrum for this occupancy is in reasonable agreement with what is observed
461 (compare a and b in Fig. 9). The agreement between the simulated and experimental spectra
462 for the edge and post-edge regions (Figs. 6 and 8) is less good but not unreasonable given the
463 complexity of the models.
464
465 To determine $Ti^{3+}/\Sigma Ti$ in hibonite by XANES spectroscopy would require a large set of well-
466 characterised standards. These standards would need to encompass not only variable $Ti^{3+}/\Sigma Ti$
467 but also different ΣTi to account for changes in the Ti site at constant $Ti^{3+}/\Sigma Ti$ and the
468 diversity of possible Ti-Ti interactions (Ti^{3+}-Ti^{3+}, Ti^{4+}-Ti^{4+}, Ti^{3+}-Ti^{4+}) across the shared face
469 of the M4 octahedra. Standards may be characterised by determining ΣTi and Mg by EPMA
470 and estimating $Ti^{3+}/\Sigma Ti$ by assuming $Ti^{4+} = Mg^{2+}$. EPMA may similarly be used to evaluate
471 $Ti^{3+}/\Sigma Ti$ of meteoritic hibonite if the amount of Si is determined accurately (Simon et al.
472 1997), although the presence of relatively small amounts of other transition metals may
473 introduce significant uncertainties.
474
475 We have shown that hibonite with almost any value of $Ti^{3+}/\Sigma Ti$ can be prepared at constant
476 fO_2 and that a constant value of $Ti^{3+}/\Sigma Ti$ can be produced over a range of fO_2. Hibonite will
477 equilibrate with a melt that contains Mg to produce a $Ti^{3+}/\Sigma Ti$ value that is independent of
478 fO_2. Meteoritic hibonite may re-equilibrate with post-formation conditions by changing its
479 Mg content and hence $Ti^{3+}/\Sigma Ti$ value. The primary factor that controls the $Ti^{3+}/\Sigma Ti$ ratio is

the availability of Mg rather than fO_2. The crystal chemistry also determines the Ti site occupancy, which varies with Ti concentration. The site occupied by Ti clearly affects the XANES spectrum and the potential for it to be used to determine $Ti^{3+}/\Sigma Ti$. Changes in site occupancy and the resulting Ti-Ti interactions will similarly affect other spectroscopic techniques, such as optical absorption, ESR, XPEEM, STXM and electron energy loss (EELS). The crystal chemistry of hibonite severely compromises its ability to record a $Ti^{3+}/\Sigma Ti$ value that relates to fO_2 or for $Ti^{3+}/\Sigma Ti$ to be quantified accurately.

Acknowledgements

We thank Dean Scott for preparing some of the samples, John Spratt for assistance with the electron microprobe analyses, Jens Najorka for recording some of the XRD patterns, Patricia Doyle for helping to acquire the XANES spectra of 10-43 and 7-981, and Diamond Light Source for providing beamtime. A.J.B. thanks the Australian Research Council for a Future Fellowship. A.N.K. and A.V.S. thank the Ministry of Education and Science of the Russian Federation for the award of grant 16.3871.2017/ПЧ ("Picometre diagnostics of parameters of 3D atomic structure of nanomaterials on the basis of XANES spectroscopy"). A.M.W. thanks the Natural Environment Research Council for an Independent Research Fellowship (NE/K008803/1). Steven Simon is thanked for his review of the manuscript.

References

Beckett, J.R., Live, D., Tsay, F.-D., Grossman, L. and Stolper, E. (1988) Ti^{3+} in meteoritic and synthetic hibonite. Geochimica et Cosmochimica Acta, 52, 1479-1495.

Beckett, J.R. and Stolper, E. (1994) The stability of hibonite, melilite and other aluminous phases in silicate melts: implications for the origin of hibonite-bearing inclusions from carbonaceous chondrites. Meteoritics, 29, 41-65.

Berry, A.J., O'Neill, H.St.C. (2004) A XANES determination of the oxidation state of chromium in silicate glasses. American Mineralogist 89, 790-798.

Berry, A.J., Walker, A.M., Hermann, J., O'Neill, H.St.C., Foran, G.J., and Gale, J.D. (2007) Titanium substitution mechanisms in forsterite. Chemical Geology, 242, 176-186.

Berry, A.J., Danyushevsky, L.V., O'Neill, H.St.C., Newville, M., and Sutton, S.R. (2008) The oxidation state of iron in komatiitic melt inclusions indicates hot Archaean mantle. Nature, 455, 960-963.

Berry, A.J., Yaxley, G.M., Woodland, A.B., and Foran, G.J. (2010) A XANES calibration for determining the oxidation state of iron in mantle garnet. Chemical Geology, 278, 31-37.

Burnham, A.D., Berry, A.J., Halse, H.R., Schofield, P.F., Cibin, G., and Mosselmans, J.F.W. (2015) The oxidation state of europium in silicate melts as a function of oxygen fugacity, composition and temperature. Chemical Geology, 411, 248-259.

Bunau, O. and Joly, Y. (2009) Self-consistent aspects of x-ray absorption calculations. Journal of Physics: Condensed Matter, 21, 345501.

Doyle, P.M., Schofield, P.F., Berry, A.J., Walker, A.M., and Knight, K.S. (2014) Substitution of Ti^{3+} and Ti^{4+} in hibonite ($CaAl_{12}O_{19}$). American Mineralogist, 99, 1369-1382.

Doyle, P.M., Berry, A.J., Schofield, P.F., and Mosselmans, J.F.W. (2016) The effect of site geometry, Ti content and Ti oxidation state on the Ti K-edge XANES spectrum of synthetic hibonite. Geochimica et Cosmochimica Acta, 187, 294-310.

Farges, F., Brown Jr., G.E., and Rehr, J.J. (1996) Coordination chemistry of Ti(IV) in silicate glasses and melts: I. XAFS study of titanium coordination in oxide model compounds. Geochimica et Cosmochimica Acta 60, 3023-3038.

Giannini, M., Boffa Ballaran, T., and Langenhorst, F. (2014) Crystal chemistry of synthetic Ti-Mg-bearing hibonites: a single-crystal X-ray study. American Mineralogist, 99, 2060-2067.

Ihinger, P.D. and Stolper, E. (1986) The color of meteoritic hibonite: an indicator of oxygen fugacity. Earth and Planetary Science Letters, 78, 67-79.

Ireland, T.R. (1988) Correlated morphological, chemical, and isotopic characteristics of hibonites from the Murchison carbonaceous chondrite. Geochimica et Cosmochimica Acta, 52, 2827-2839.

552
553 Ireland, T.R. (1990) Presolar isotopic and chemical signatures in hibonite-bearing refractory
554 inclusions from the Murchison carbonaceous chondrite. Geochimica et Cosmochimica Acta,
555 54, 3219-3237.
556
557 Ireland, T.R., Zinner, E.K., Fahey, A.J., and Esat, T.M. (1992) Evidence for distillation in the
558 formation of HAL and related hibonite inclusions. Geochimica et Cosmochimica Acta, 56,
559 2503-2520.
560
561 Jerebtsov, D.A. and Mikhailov, G.G. (2001) Phase diagram of CaO-Al_2O_3 system. Ceramics
562 International, 27, 25-28.
563
564 Joly, Y. (2001) X-ray absorption near edge structure calculations beyond the muffin-tin
565 approximation. Physical Review B, 63, 125120.
566
567 Kornacki, A.S. and Fegley, B. Jr. (1986) The abundance and relative volatility of refractory
568 trace elements in Allende Ca,Al-rich inclusions: implications for chemical and physical
569 processes in the solar nebula. Earth and Planetary Science Letters, 79, 217-234.
570
571 Larson, A.C. and Von Dreele, R.B. (1994) General Structure Analysis System (GSAS), Los
572 Alamos National Laboratory Report. LAUR 86-748 (revised version).
573
574 Lodders, K. (2003) Solar System abundances and condensation temperatures of the elements.
575 Astrophysical Journal, 591, 1220-1247.
576
577 Mosselmans, J.F., Quinn, P.D., Dent, A.J., Cavill, S.A., Moreno, S.D., Peach, A., Leicester,
578 P.J., Keylock, S.J., Gregory, S.R., Atkinson, K.D., and Rosell, J.R. (2009) I18 - the
579 microfocus spectroscopy beamline at the Diamond Light Source. Journal of Synchrotron
580 Radiation, 16, 818-824.
581
582 Nakamura, T.M., Sugiura, N., Kimura, A., Miyazaki, A, and Krot, A.N. (2007) Condensation
583 and aggregation of solar corundum and corundum-hibonite grains. Meteoritics and Planetary
584 Science, 42, 1249-1265.
585
586 Rout, S. and Bischoff, A. (2008) Ca,Al-rich inclusions in Rumuruti (R) chondrites.
587 Meteoritics and Planetary Science, 43, 1439-1464.

588
589 Schofield, P.F., Smith, A.D., Scholl, A., Doran, A., Covey-Crump, S.J., Young, A.T., and
590 Ohldag, H. (2014) Chemical and oxidation-state imaging of mineralogical intergrowths: The
591 application of X-ray Photo-Emission Electron Microscopy (XPEEM). Coordination
592 Chemistry Reviews, 277-278, 31-43.
593
594 Simon, S.B., Grossman, L., and Davis, A.M. (1997) Multiple generations of hibonite in
595 spinel-hibonite inclusions from Murchison. Meteoritics and Planetary Science, 32, 259-269.
596
597 Simon, S.B., Davis, A.M., Grossman, L., and McKeegan, K.D. (2002) A hibonite-corundum
598 inclusion from Murchison: a first-generation condensate from the solar nebula. Meteoritics
599 and Planetary Science, 37, 533-548.
600
601 Simon, S.B., Sutton, S.R., and Grossman, L. (2007) Valence of titanium and vanadium in
602 pyroxene in refractory inclusion interiors and rims. Geochimica et Cosmochimica Acta, 71,
603 3098-3118.
604
605 Tailby, N.D., Walker, A.M., Berry, A.J., Hermann, J., Evans, K.A., Mavrogenes, J.A.,
606 O'Neill, H.St.C., Rodina, I.S., Soldatov, A.V., Rubatto, D., and Sutton, S.R. (2011) Ti site
607 occupancy in zircon. Geochimica et Cosmochimica Acta, 75, 905-921.
608
609 Toby, B.H. (2001) EXPGUI, a graphical user interface for GSAS. Journal of Applied
610 Crystallography, 34, 210-221.
611
612 Yamaga, M., Yosida, T., Hara, S., Kodama, N., and Henderson, B. (1994) Optical and
613 electron spin resonance spectroscopy of Ti^{3+} and Ti^{4+} in Al_2O_3. Journal of Applied Physics,
614 75, 1111–1117.
615
616 Yoneda, S. and Grossman, L. (1995) Condensation of CaO-MgO-Al_2O_3-SiO_2 liquids from
617 cosmic gases. Geochimica et Cosmochimica Acta, 59, 3413-3444.
618
619
620 **Figure Captions**
621
622 Figure 1: (a) *c* lattice parameter and (b) *V*, unit cell volume, as a function of Ti pfu,
623 determined for synthetic hibonite ($CaAl_{12-2x}Mg_xTi^{4+}_xO_{19}$) in this study (circles), and from

624 Doyle et al. 2014 (squares) and Giannini et al. 2014 (triangles). Samples with $Ti^{3+}/\Sigma Ti = 0$
625 are denoted by solid symbols and those containing Ti^{3+} by open symbols. Error bars are
626 smaller than the symbols.
627
628 Figure 2: Ti^{4+} on (a) M4 in pfu and (b) M2/M4, as a function of Ti^{4+} pfu for synthetic hibonite
629 in this study (circles), Doyle et al. 2014 (squares), and Giannini et al. 2014 (triangles).
630 Samples with $Ti^{3+}/\Sigma Ti = 0$ are denoted by solid symbols and those containing Ti^{3+} by open
631 symbols. The error bars are smaller than the symbols except where shown.
632
633 Figure 3: FE-SEM BSE images of hibonite crystals (dark) in melt of CAI composition
634 produced by equilibrating (a) (0.15, 1.0) in melt A at IW-4.3 and (c) (0.15, 1.0) in melt B at
635 IW-3.3. (b) Ti, Ca, and Al composite elemental map, highlighting the distribution of Ti in a
636 crystal of hibonite, of the area indicated by the box in (a). Elemental maps corresponding to
637 the area indicated by the box in (c) are shown for (d) Al, (e) Ti, and (f) Mg. The scale bars in
638 (a) and (c) are 20 μm and those in (b) and (d) are 2 μm.
639
640 Figure 4: Variations of SiO_2 (circles) and MgO (squares) determined by EPMA as a function
641 of distance from the edge to centre of a crystal of hibonite in glass for sample (0.30, 1.0)
642 equilibrated with melt A at IW-2.3. The values at Position = 5 μm are reported in Table 2.
643
644 Figure 5: (a) *c* lattice parameter of hibonite and (b) wt% hibonite determined by QPA of
645 samples obtained by equilibrating oxides corresponding to the hibonite compositions (0.98,
646 0.0) (open squares), (0.62, 0.6) (solid circles) and (0.33, 1.0) (open circles) at 1400 ˚C and
647 various values of $\log f O_2$ relative to the IW buffer. Error bars are smaller than the symbols.
648
649 Figure 6: Ti K-edge XANES spectra of natural hibonite samples (a) 10-43 (0.55 Ti pfu) and
650 (c) 7-981 (0.1 Ti pfu) from the Murchison carbonaceous chondrite, and synthetic hibonite
651 with compositions (b) (0.44, 0.0) and (d) (0.1, 0.0). Spectra are offset for clarity.
652
653 Figure 7: The pre-edge region of Ti K-edge XANES spectra of natural hibonite samples (a)
654 10-43 (0.55 Ti pfu) and (b) 7-981 (0.1 Ti pfu) from the Murchison carbonaceous chondrite,
655 and synthetic hibonite with compositions (c) (0.1, 0.0), (d) (0.2, 0.0), (e) (0.3, 0.0), (f) (0.44,
656 0.0), (g) (0.98, 0.0), and (h) (0.2, 1.0). Spectra are offset for clarity.
657
658 Figure 8: Simulated Ti K-edge XANES spectra of hibonite, modelled using FDMNES, with

(a) Ti^{4+} on M2, (b) Ti^{4+} on M4, (c) Ti^{4+} clustered on adjacent M4, (d) Ti^{4+} on M2 (20%) and Ti^{4+} clustered on adjacent M4 (80%), (e) Ti^{3+} on M2, and (f) Ti^{3+} clustered on adjacent M4. Spectra are offset for clarity.

Figure 9: The pre-edge region of the Ti K-edge XANES spectrum of (a) natural hibonite sample 10-43, and simulated spectra, modelled using FDMNES, of hibonite with (b) Ti^{4+} on M2 (20%) and Ti^{4+} clustered on adjacent M4 (80%), (c) Ti^{4+} clustered on adjacent M4, (d) Ti^{4+} on M4, and (e) Ti^{4+} on M2. Spectra are offset for clarity.

Figure 10: Correlation between Mg and Ti + Si pfu for hibonite crystals equilibrated in a CAI composition melt at 1450 ˚C and the values of fO_2, in log units relative to the IW buffer, indicated. The line is the best fit to the data and has a slope of ~ 0.8.

Table 1: Lattice parameters and Mg and Ti site occupancies (as fractions of 1) of synthetic hibonite with $Ti^{3+}/\Sigma Ti = 0$ determined by Rietveld refinement of XRD data. Ti^{4+} (M4) was calculated assuming that Ti^{4+} pfu = Mg^{2+} pfu.

Sample	*a* (Å)	*c* (Å)	Volume (Å^3)	Mg (M3)	Ti^{4+} (M2*)	Ti^{4+} (M4)	Ti^{4+} (M2/M4)
(0.0, 0.0)	5.55769(2)	21.8958(2)	585.708(4)	-	-	-	-
(0.10, 0.0)	5.56305(2)	21.9095(1)	587.204(3)	0.05	0.035(5)	0.015(5)	2.33(84)
(0.20, 0.0)	5.56790(2)	21.92436(9)	588.627(3)	0.10	0.050(5)	0.050(5)	1.00(14)
(0.30, 0.0)	5.57443(2)	21.9430(1)	590.512(3)	0.15	0.065(5)	0.085(5)	0.76(7)
(0.40, 0.0)	5.58060(2)	21.9653(1)	592.419(3)	0.20	0.075(5)	0.125(5)	0.60(5)
(0.44, 0.0)	5.58874(7)	21.9986(6)	595.05(1)	0.21	0.05(1)	0.16(2)	0.31(7)
(0.98, 0.0)	5.6065(1)	22.0700(5)	600.79(3)	0.48	0.136(7)	0.34(1)	0.40(2)

*Site is half occupied.

Table 2: Compositions of hibonite crystals, expressed as wt% oxide and cations per formula unit for 19 oxygens, after equilibration of $CaAl_{12-y}Ti^{3+}_{y}O_{19}$ ($Ti^{3+}/\Sigma Ti = 1$) hibonite with melt composition A or B at various values of $\log f O_2$ relative to the IW buffer. $Ti^{3+}/\Sigma Ti$ was calculated from stoichiometry assuming $Ti^{4+} = Mg$ and $Ti^{4+} + Si = Mg$. For some experiments two different hibonite compositions were identified.

Hibonite	Melt	ΔIW	CaO	Al_2O_3	MgO	TiO_2	SiO_2	Total	Ca	Al	Mg	Ti	Si	Total	$Ti^{3+}/\Sigma Ti$ $Ti^{4+}=Mg$	$Ti^{3+}/\Sigma Ti$ $Ti^{4+}+Si=Mg$
			wt % (±0.02)						pfu (±0.01)							
(0.30, 1.0)	A	-0.3	9.45	82.98	1.66	3.60	0.96	98.64	1.15	11.15	0.28	0.31	0.11	13.01	0.09(5)	0.44(6)
(0.30, 1.0)	A	-1.3	8.69	84.15	1.80	3.72	0.34	98.71	1.06	11.28	0.31	0.32	0.04	13.00	0.04(4)	0.16(5)
(0.30, 1.0)	B	-1.3	8.87	86.18	1.38	2.78	0.29	99.51	1.07	11.44	0.23	0.24	0.03	13.01	0.02(6)	0.15(7)
(0.30, 1.0)	A	-2.3	8.83	84.12	1.77	3.87	0.32	98.91	1.07	11.26	0.30	0.33	0.04	13.00	0.09(4)	0.20(5)
(0.25, 1.0)	B	-2.3	9.06	87.17	0.65	1.03	0.54	98.46	1.10	11.66	0.11	0.09	0.06	13.02	0.00(16)	0.45(20)
(0.15, 1.0)	A	-3.3	9.20	85.78	1.34	2.80	0.46	99.58	1.11	11.39	0.23	0.24	0.05	13.02	0.05(6)	0.27(7)
(0.15, 1.0)	A	-3.3	9.02	85.46	1.50	3.36	0.47	99.82	1.09	11.33	0.25	0.28	0.05	13.00	0.12(5)	0.30(6)
(0.15, 1.0)	B	-3.3	8.93	88.60	0.67	1.36	0.14	99.70	1.07	11.70	0.11	0.11	0.02	13.02	0.02(10)	0.16(15)
(0.15, 1.0)	B	-3.3	8.79	84.32	1.66	3.64	0.23	98.63	1.07	11.31	0.28	0.31	0.03	13.01	0.10(5)	0.18(5)
(0.30, 1.0)	A	-3.3	9.21	88.31	0.64	1.24	0.37	99.77	1.11	11.66	0.11	0.10	0.04	13.02	0.00(12)	0.37(17)
(0.30, 1.0)	A	-4.3	8.81	85.35	1.54	3.46	0.23	99.38	1.07	11.36	0.26	0.29	0.03	13.00	0.12(5)	0.21(6)
(0.15, 1.0)	A	-6.3	9.17	87.98	0.54	1.32	0.15	99.16	1.11	11.70	0.09	0.11	0.02	13.02	0.19(13)	0.34(15)
(0.15, 1.0)	A	-6.3	9.03	85.99	1.24	2.92	0.28	99.47	1.09	11.43	0.21	0.25	0.03	13.01	0.16(6)	0.29(7)
(0.15, 1.0)	B	-6.3	9.32	87.72	0.89	1.65	0.69	100.27	1.11	11.54	0.15	0.14	0.08	13.02	0.00(10)	0.49(13)
(0.25, 1.0)	A	-6.3	9.01	83.56	1.76	4.33	0.34	99.01	1.10	11.19	0.30	0.37	0.04	13.00	0.19(4)	0.30(5)
(0.25, 1.0)	A	-6.3	8.95	85.52	1.07	2.85	0.41	98.80	1.09	11.43	0.18	0.24	0.05	12.99	0.26(6)	0.45(7)

Table 3: Lattice parameters of hibonite and the proportion of phases (wt %), determined by Rietveld QPA refinement, obtained after equilibrating three hibonite compositions at 1400 ˚C and various values of log$f$O$_2$ relative to the IW buffer.

Composition	ΔIW	*a* (Å)	*c* (Å)	Volume (Å^3)	hibonite	$CaTiO_3$	$MgAl_2O_4$	Al_2O_3	Al_2TiO_5	TiO	TiO_2
(0.33, 1.0)											
	-6.3	5.56676(6)	21.9471(3)	589.00(2)	98.9(4)	-	-	-	-	1.1(1)	-
	-2.3	5.56448(5)	21.9363(4)	588.23(1)	61.5(3)	5.5(1)	-	32.0(2)	1.0(1)	-	-
	-0.3	5.56566(5)	21.9384(4)	588.53(1)	51.0(3)	6.0(1)	-	42.0(2)	1.0(1)	-	-
	2.3	5.56417(5)	21.9330(4)	588.07(1)	49.1(3)	6.3(1)	-	43.2(2)	1.4(1)	-	-
	4.3	5.56476(6)	21.9348(5)	588.24(1)	48.2(3)	6.2(1)	-	43.9(2)	1.7(1)	-	-
	7.3	5.56472(5)	21.9345(4)	588.23(1)	51.0(3)	6.3(1)	-	41.3(2)	1.4(1)	-	-
(0.62, 0.6)											
	-6.3	5.57720(4)	21.9850(3)	592.23(1)	93.8(4)	0.9(1)	-	4.9(1)	-	0.4(1)	-
	-2.3	5.57725(3)	21.9686(3)	591.80(1)	97.0(3)	3.0(1)	-	-	-	-	-
	-0.3	5.57634(3)	21.9609(3)	591.40(1)	95.5(4)	0.6(1)	-	-	3.9(1)	-	-
	2.3	5.57527(3)	21.9614(3)	591.18(1)	97.1(3)	-	-	-	2.9(1)	-	-
	4.3	5.57470(3)	21.9561(2)	590.92(1)	95.7(3)	-	-	-	4.3(1)	-	-
	7.3	5.57511(3)	21.9616(3)	591.15(1)	97.9(3)	-	-	-	2.1(1)	-	-
(0.98, 0.0)											
	-6.3	5.60052(8)	22.0532(7)	599.04(4)	87.1(4)	3.1(1)	8.8 (1)	-	-	-	1.0(1)
	-2.3	5.60843(6)	22.0745(5)	601.32(1)	93.0(4)	2.1(1)	4.5 (1)	0.4(1)	-	-	-
	2.3	5.60949(4)	22.0843(4)	601.81(1)	96.1(4)	1.4(1)	2.0 (1)	-	0.5(1)	-	-
	4.3	5.60959(3)	22.0843(5)	601.83(1)	97.2(3)	1.1(1)	1.7 (1)	-	-	-	-
	7.3	5.60886(4)	22.0856(4)	601.71(1)	96.0(3)	1.7(1)	2.3 (1)	-	-	-	-

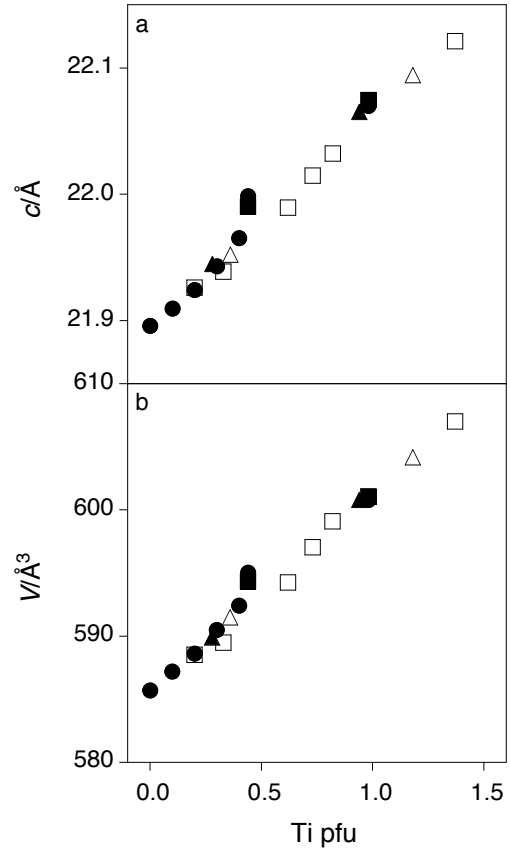

Figure 1

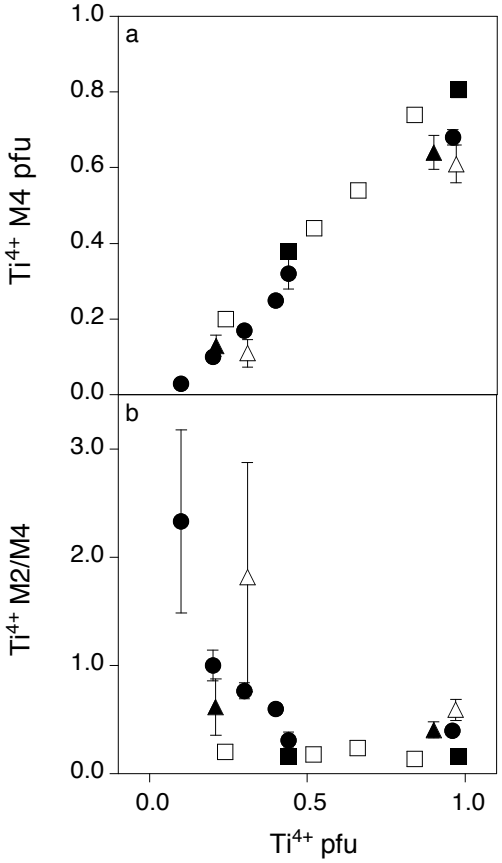

Figure 2

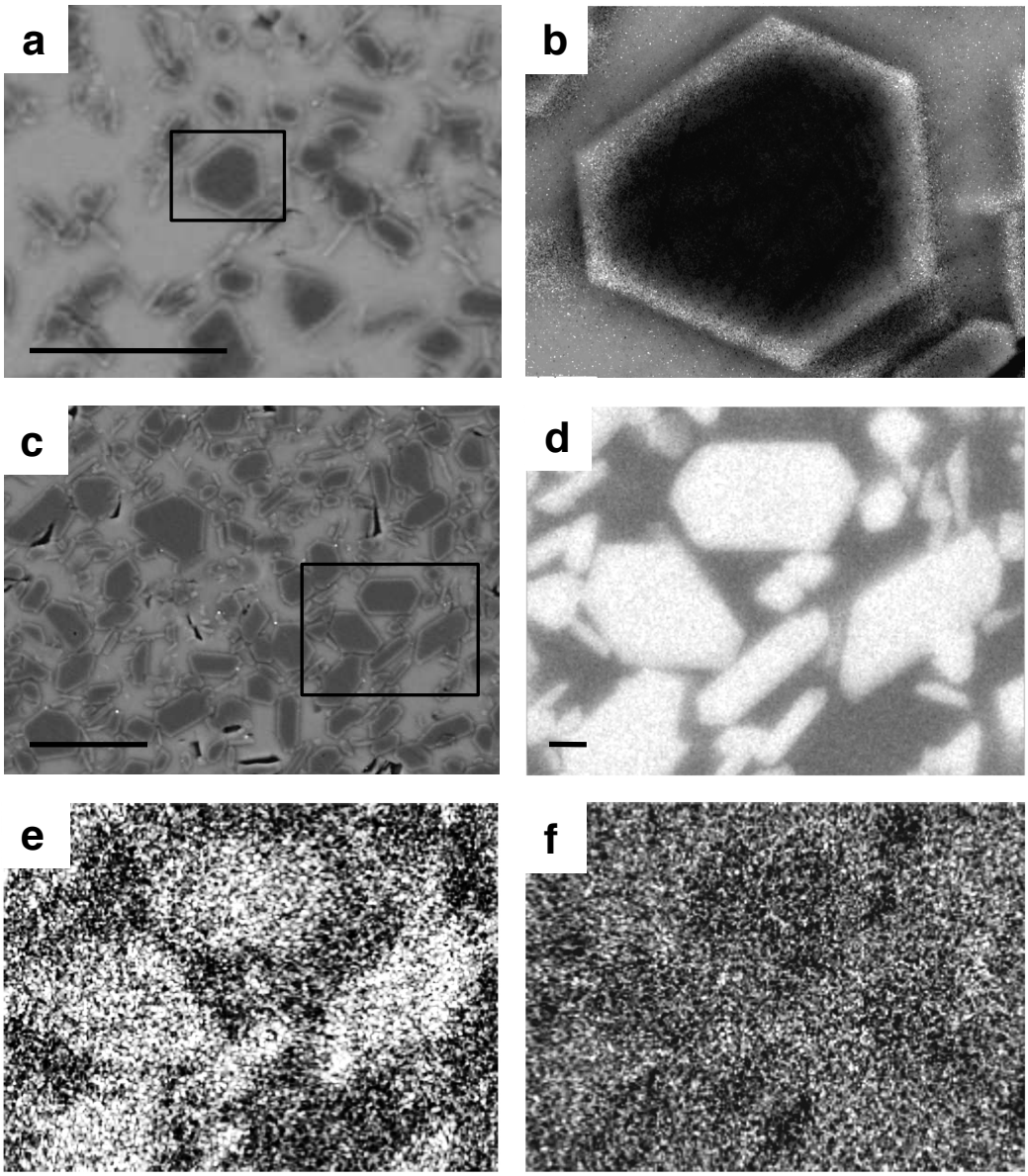
a
b
c
d
e
f

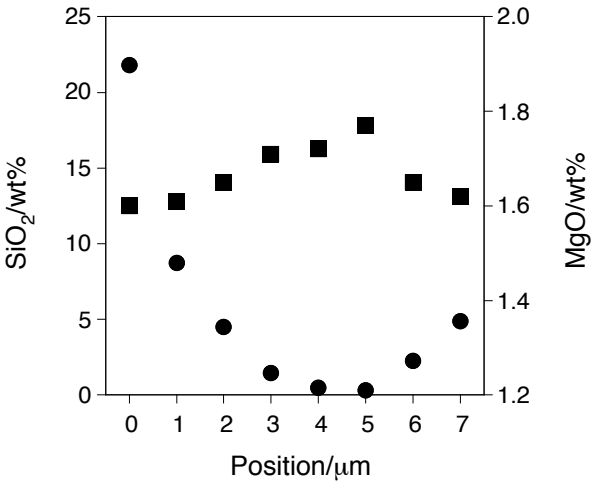

Figure 4

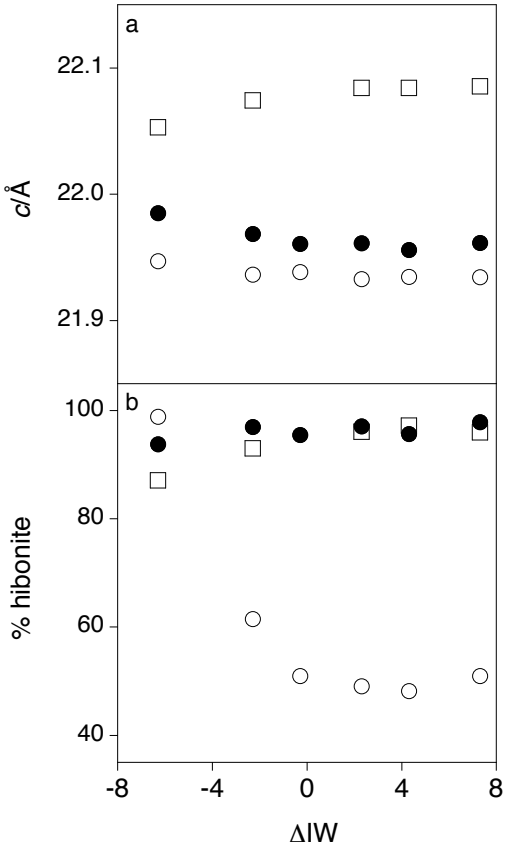

Figure 5

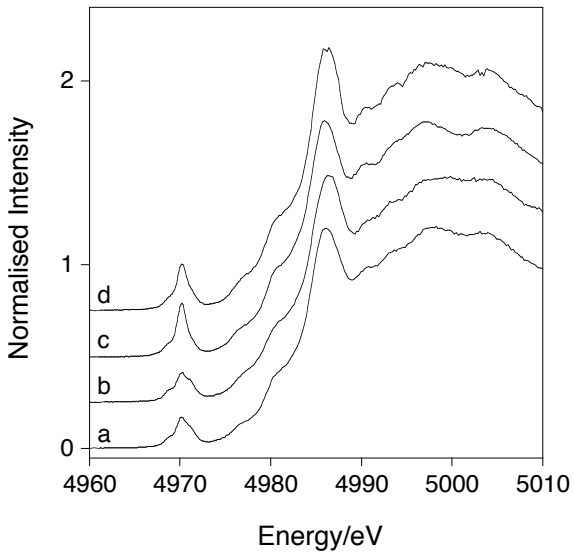
Normalised Intensity
2
1
0
d
c
b
a
4960
4970
4980
4990
5000
5010
Energy/eV

Figure 6

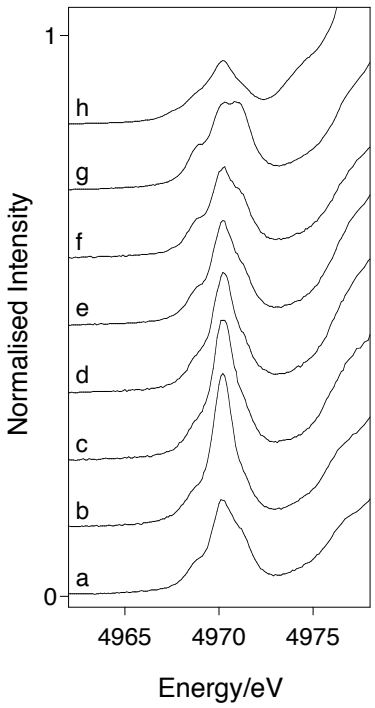

Figure 7

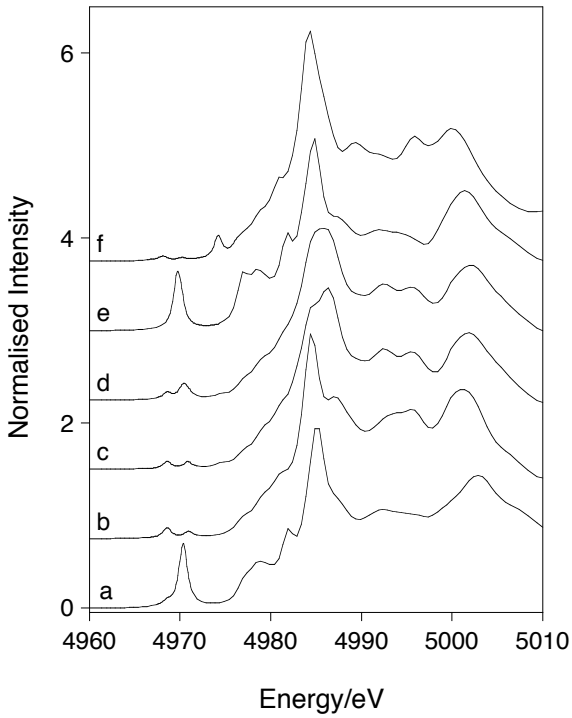
Normalised Intensity
0
2
4
6
a
b
c
d
e
f
4960
4970
4980
4990
5000
5010
Energy/eV

Figure 8

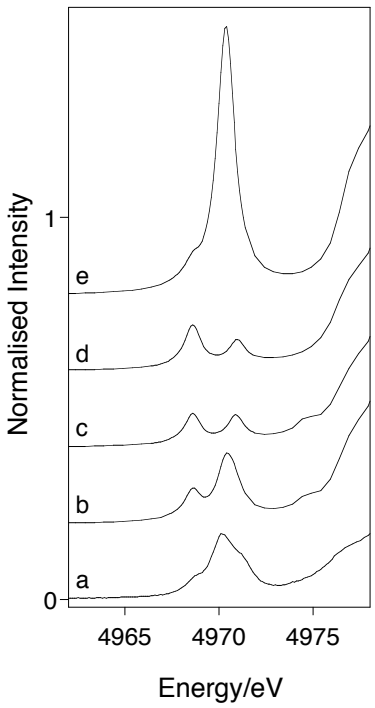

Figure 9

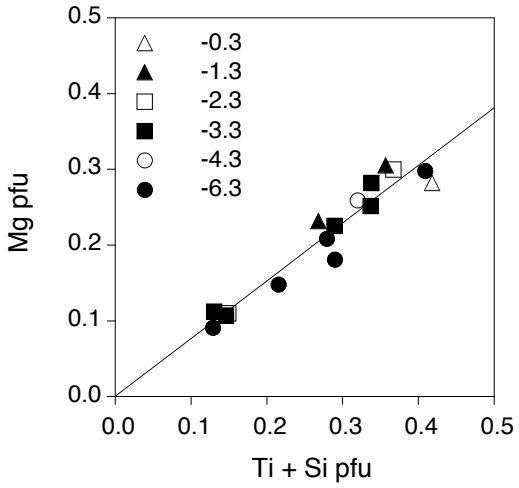

Figure 10